

A fiber-loop laser with a cooled erbium-doped section

Eyal Buks*

Andrew and Erna Viterbi Department of Electrical Engineering, Technion, Haifa 32000, Israel

Boris A. Malomed†

Instituto de Alta Investigación, Universidad de Tarapacá, Casilla 7D, Arica, Chile

(Dated: September 16, 2025)

An optical comb featuring an unusual structure has been recently observed in a fiber-loop laser running at cryogenic temperatures. In the present work, the effect of optical polarization on the operation of the laser is explored. Multi-mode lasing with a relatively high degree of inter-mode coherency is experimentally demonstrated. The setup can be used for applications to spectroscopy, communications, and quantum data storage.

Introduction – Erbium doped fibers (EDFs) are widely employed in many applications. An important aspect of the work with EDF is that its key properties may strongly depend on the temperature [1–7]. In particular, at cryogenic temperatures, an EDF can be used for storing quantum information [8–14]. Storage times exceeding 10 seconds [15, 16] have been achieved by implementing the method of persistent spectral hole burning. Furthermore, a properly cooled EDF can support robust multi-mode lasing regime. The latter feature is important as multimode lasing finds diverse applications to spectroscopy, signal processing, and communications [17, 18]. Multimode lasing in the telecom band has been demonstrated by an EDF cooled with liquid nitrogen [19–21]. At still lower temperatures, an unequally spaced optical comb (USOC) can be generated by a fiber loop laser with an integrated EDF [22], see Fig. 2(b) below. However, the mechanism responsible for the formation of the USOC in that setup remains unknown. Actually, the USOC may be considered as the extreme opposite to a regular optical comb, in which the frequency spacings between adjacent peaks are all identical. In contrast, the frequency spacings between all pairs of USOC peaks are unique.

The current study addresses effects of optical polarization on the operation of the laser. A high degree of polarization (DOP) is propitious for some potential USOC-based applications. We explore the effect of polarization by integrating a polarization filter (PF) and polarization controllers (PC) into the fiber loop, see Fig. 1 (a). We find that the inserted components enable USOC formation with a relatively high DOP, as shown in Fig. 5. The enhanced DOP is used for the generation of frequency-tunable radio-frequency (RF) tones through coherent beating between pairs of USOC peaks, as shown in Fig. 6 below. Moreover, the inserted polarization-controlling ingredients allow tuning the fiber loop into a mode-locking phase [23, 24], see Fig. 4 below.

Experimental setup – A sketch of the unidirectional

fiber loop laser under the study is presented in Fig. 1(a). The loop is made of $l_{\text{EDF}} = 5$ m long EDF, and an undoped single-mode fiber (Corning 28). The EDF absorption is 30 dB^{-1} at 1530 nm , and the mode field diameter is $6.5 \mu\text{m}$ at 1550 nm . A wavelength-division multiplexing (WDM) device is used to integrate the EDF, which is installed inside a cryostat, with a unidirectional room-temperature fiber loop. The EDF is pumped by a 980 nm laser diode (LD), biased with current I_D . A 10:90 optical coupler (OC), and two isolators [labeled by arrows in the sketch shown in Fig. 1(a)], are integrated into the fiber loop. The output port of the 10:90 OC is connected to a polarimeter optical spectrum analyzer (POSA) [25], and to a photo-detector (PD), which is probed by both a radio-frequency spectrum analyzer (RFSa) and an oscilloscope (OS). An optional optical filter (OF) with a central wavelength λ_F and linewidth 1.2 nm (the full width at half maximum) can be installed between the 10:90 OC and the PD. The OF is installed and used only for the measurements presented below in Fig. 6.

The dependence on diode current I_D is shown in Fig. 2. For all measurements presented by Fig. 2, the EDF temperature is 2.8 K . The measured PD averaged voltage V_{PD} (proportional to the averaged optical power) is plotted in Fig. 2(a) as a function of I_D . Below a critical temperature of about 14 K USOC becomes visible in the optical spectrum. The USOC sequence shown in Fig. 2(b) is measured with diode current of I_{D1} [see Fig. 2(a)].

USOC – The underlying mechanism responsible for the USOC formation [see Fig. 2(b)] has remained mainly unknown [26]. This effect is partially attributed to the temperature dependence of the EDF emission and absorption rates [27]. It has been shown that the effective normalized EDF length, η_{EDF} , which is defined as $\eta_{\text{EDF}} = l_{\text{EDF}} / (l_E \log \alpha_{\text{FL}})$, where l_E is the EDF emission length, and α_{FL} is the loss coefficient of the fiber loop, becomes significantly smaller than unity in the low temperature region, in which USOC is formed [26]. This transition from long to short EDF (i.e., from $\eta_{\text{EDF}} \gg 1$ to $\eta_{\text{EDF}} \ll 1$) is demonstrated by the open-loop measurements displayed in Figs. 1(c) and (d). In these measurements, a low-resolution optical spectrum analyzer (OSA),

*Electronic address: eyal@ee.technion.ac.il

†Electronic address: malomed@tauex.tau.ac.il

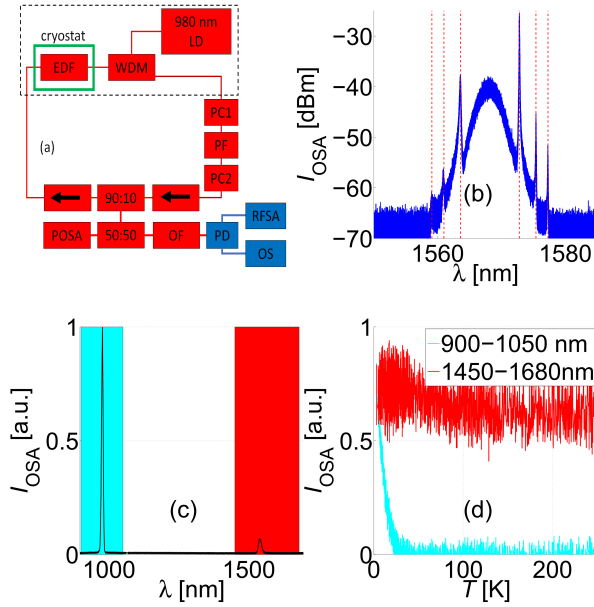


FIG. 1: The experimental setup. (a) Optical components and fibers are red colored, whereas the blue color is used to label the RF components and coaxial cables. The dashed rectangle labels the part of the setup used for the open-loop transmittance measurement, which are presented in panels (c) and (d). (b) POSA measurement of the optical spectrum with diode current of $I_D = 0.8$ A (the corresponding diode power is $P_D = 480$ mW). The Kelly sidebands [see Eq. (2)] are labeled by overlaid vertical dashed lines. (c) Optical spectrum at temperature 2.9 K. This measurement is performed in the open-loop configuration, with a low-resolution OSA connected to the left end of the EDF. The diode current is $I_D = 0.25$ A and the power is $P_D = 160$ mW. (d) The integrated optical spectrum as a function of temperature for the pumping band 900–1050 nm [see the cyan rectangle in (c)] and telecom band 1450–1680 nm [see the red rectangle in (c)].

connected to the left end of the EDF, is used to measure the EDF transmittance. As seen from the plot in Fig. 1 (c-d), the open-loop transmittance near the pump wavelength of 980 nm is significantly enhanced at low temperatures. The enhancement, which was reported previously in Ref. [28], is attributed to the increase of the lifetime of excited states at low temperatures [29, 30], which, in turn, gives rise to a reduction in the saturation value of the pump power.

The USOC n -th peak wavelength is denoted by λ_n , with $n = 0, 1, 2, \dots$. The frequency associated with the n -th peak is $f_n = c/\lambda_n$, where c is the speed of light in vacuum, and the corresponding normalized frequency detuning is $i_n \equiv (f_0 - f_n)/f_L$, where $f_L = c/(n_F l_L)$ is the loop frequency, $n_F = 1.45$ is the fiber's refractive group index, and l_L is the total length of the fiber loop. The detuning sequence $\{i_n\}$ is found to be well fitted by an empirical law given by [22]

$$i_n = \nu \log p_n, \quad (1)$$

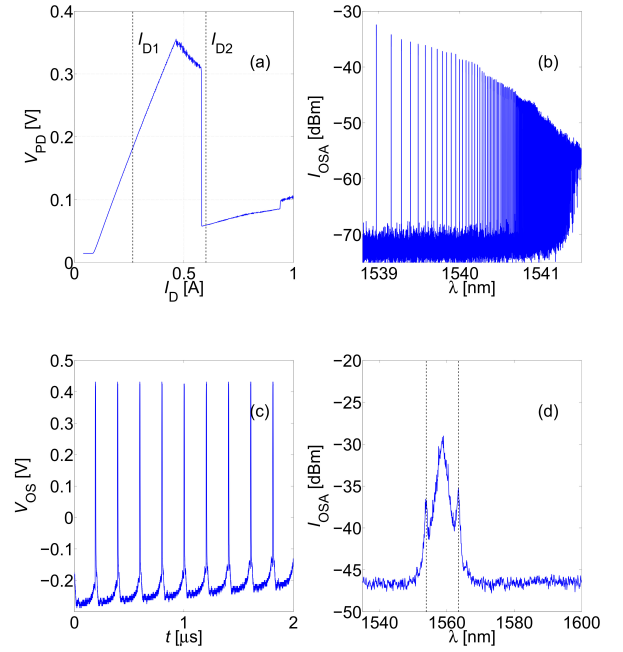


FIG. 2: Fiber-loop. The temperature is 2.8 K. (a) The dependence of the measured PD averaged voltage V_{PD} on diode current I_D . (b) USOC optical spectrum. (c) Optical pulses measured by the OS. (d) Optical spectrum in the mode-locking regime. The diode current is I_{D1} in (b) and I_{D2} in (c) and (d).

where ν is a positive constant, and p_n is the n -th prime number. The degree of the agreement between the data and empiric law (1) has been evaluated in Ref. [26].

USOC is highly sensitive to perturbations applied in the spectral band close to the loop frequency f_L . This is experimentally demonstrated by installing an electro-optic modulator (EOM) into the fiber loop. The optical and RF spectra are shown as a function of modulation frequency, f_{FG} , in plots (a) and (b), respectively, of Fig. 3 (for these measurements, the loop frequency is $f_L = 5.466$ MHz). Note that EOM is installed in the fiber loop only for the measurements shown in Fig. 3.

Mode locking – The fiber loop under the study can be tuned into the mode-locking regime. Current I_{D2} is applied for the measurements shown in Figs. 2(c) and (d), which display a time trace (measured with the use of the OS), and an optical spectrum, respectively, in the region where the mode locking occurs (in these measurements, the OF is removed from the experimental setup). The values I_{D1} and I_{D2} are denoted by the overlaid vertical dashed lines in Fig. 2(a). The Kelly sidebands [31–34] are labeled in Fig. 2(d) by overlaid vertical dashed lines [see also Fig. 1(b)]. While USOC is observed only at low temperatures, the mode-locking is visible in the entire range from the room to base temperatures [provided that a temperature-dependent adjustment is applied to both polarization controllers PC1 and PC2].

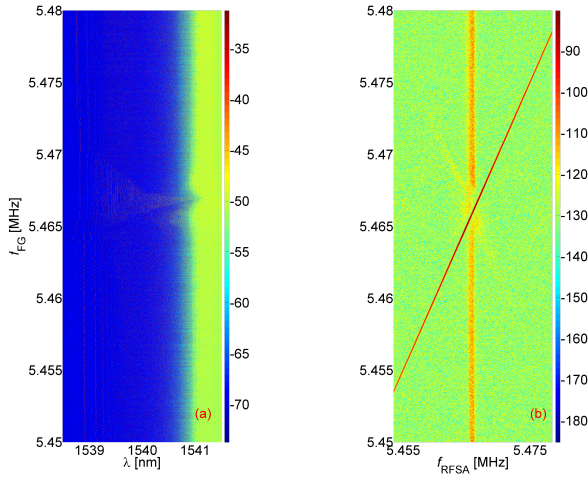


FIG. 3: EOM. (a) The optical spectrum measured by the POSA. (b) the RF spectrum measured by the RFSA. The modulation frequency f_{FG} is scanned near the loop frequency $f_L = 5.466$ MHz. The temperature is 2.8 T, the diode current is $I_D = 120$ mA, and the EOM amplitude modulation depth is 0.5%. In both (a) and (b), the spectral power is presented in dBm.

The angular-frequency shift ω_m of the m -th Kelly side-band is

$$\omega_m^2 = 2\pi\omega_{GDD}^2 m - t_p^{-2}, \quad (2)$$

where m is a positive integer, and the angular frequency ω_{GDD} is given by $\omega_{GDD}^{-2} = \beta_{2,EDF}l_{EDF} + \beta_{2,SMF}l_{SMF}$. The group delay dispersion (GDD) coefficient β_2 is $\beta_{2,SMF} = 18 \text{ ps}^2 \text{ km}^{-1}$ for the undoped single-mode-fiber (SMF) section of the loop, and $\beta_{2,EDF} = 26 \text{ ps}^2 \text{ km}^{-1}$ for the EDF section, l_{EDF} and l_{SMF} are, respectively, the EDF and SMF lengths, and t_p is the pulse width. The overlaid vertical dashed lines in Fig. 1(b) are calculated with the pulse width fitting value of $t_p = 0.62$ ps.

Note that mode locking was not found after removing the PF from the fiber loop (the search for mode locking was performed by varying the EDF temperature, the diode current I_D , and both PC1 and PC2 computer-controlled settings). This observation suggests that the underlying mechanism responsible for the mode locking in our setup is the nonlinear polarization rotation [24].

The nonlinear Schrödinger equation – Some experimental results can be accounted for with the help of a simple model, in which the light circulating in the fiber loop is represented by a scalar field $\psi(t, T)$, which depends on the retarded time t and the time T [33, 35]. The evolution is modeled by the nonlinear Schrödinger equation (NLSE) [36, 37] [see Eq. (A1) in appendix A]:

$$i \frac{d\psi}{dT} = f_L \left(i\mathcal{G} + D \frac{\partial^2}{\partial t^2} + M |\psi|^2 \right) \psi. \quad (3)$$

The net linear gain (the gain minus the loss) \mathcal{G} is real, and the complex coefficients $D = D_2 + iD_f$ and $M =$

$M_\delta + iM_\gamma$ characterize, respectively, the linear and cubic nonlinear response (M is proportional to the fiber's third-order susceptibility [33]), where $D_2 = \beta_2 / (2f_L)$ is a normalized GDD coefficient, D_f is the filter dispersion, M_δ is the self-phase modulation (SPM) coefficient [38], and M_γ is the nonlinear gain coefficient [39, 40]. For $M_\delta < 0$ ($M_\delta > 0$) self-focusing (self-defocusing) occurs. For saturable absorption (SA) one has $M_\gamma > 0$, whereas $M_\gamma < 0$ occurs under the action of the reverse saturable absorption (RSA). In the fiber-loop laser, SA commonly promotes the mode locking and the formation of optical pulses [41–43], whereas effects which give rise to RSA (e.g., two-photon absorption) suppress the mode locking [44]. The changeover from SA to RSA has been observed in Ref. [45].

Modeling the mode-locking by dint of the NLSE (3) is reviewed in appendices B and C. Further, it is shown in appendices D and E that the NLSE (3) can account for the USOC formation, provided that some assumptions are applicable. In particular, the possibility to disregard both the SPM and dispersion (i.e., setting $M_\delta = 0$ and $D = 0$) is considered in appendix E. However, these assumptions are found to be inconsistent with our experimental results (see appendix E).

The evolution of the pulse with the pump switched off – The role played by the nonlinear response in establishing the mode-locking is explored by modulating the diode current I_D . For the plots shown in Fig. 4, the modulation abruptly switches off the pump at time $t = 0$. The subsequent decay was monitored using three PDs. Figure 4(a) displays voltage V_P across a PD monitoring the optical power emitted from the 980 nm diode. The fiber-loop signal decay is monitored by two PDs. The signal measured by the faster one (having bandwidth of 1 GHz), which is capable to resolve individual optical pulses, is shown in (b), whereas the plot in (c) is obtained using the slower one (having bandwidth of 10 kHz). The comparison between the plots (b) and (c) reveals that the optical power (c) decays significantly faster than the pulses' amplitude [which is visible in (b)]. This observation is attributed to pulse narrowing which occurs in the course of the decay.

The overlaid red dashed line in Fig. 4(c) represents a fitting to an empirical relation

$$I(t) = \frac{I_s}{1 + \frac{I_s - I_0}{I_0} e^{\frac{t}{t_d}}}. \quad (4)$$

The decay function $I(t)$ given by Eq. (4) is derived from the logistic differential equation $dI/dt = -t_d^{-1} (1 - I/I_s) I$, where t_d and I_s represent the linear decay time and saturation intensity, respectively, and $I_0 = I(t=0)$. The fit yields a positive value for the parameter I_s (see the caption to Fig. 2), which is consistent with the assumption that SA occurs in the optical band where mode locking is observed.

For the case where both D and M are pure real, the narrowing effect can be analytically modeled, provided

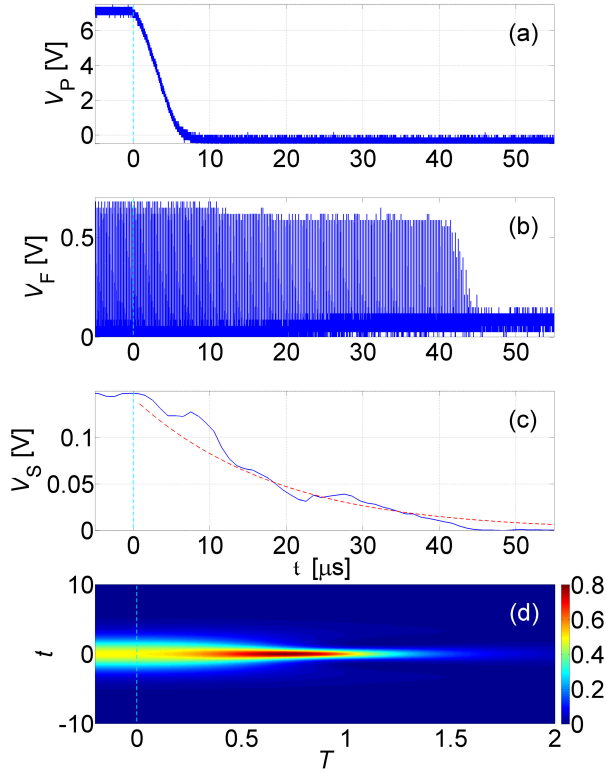


FIG. 4: The evolution of pulses with the pump switched off. Temperature is 3.2 K, and diode current prior to cutting off the pump at $t = 0$ is $I_D = 0.7$ A. The pump power is shown in (a), and the fiber-loop optical intensity in (b) and (c). The frequency bandwidth of the photo detectors used in (a), (b) and (c), is 100 kHz, 1 GHz and 10 kHz, respectively. The overlaid red dashed line in (c) represents the decay function $I(t)$ defined in Eq. (4). Assumed parameters' values are $t_d = 17 \mu s$ and $I_s/I_0 = 10$. (d) The optical intensity $|\psi|^2$ is produced by the numerical solution of the NLSE (3). Assumed parameters' values are $W = 2$, $1/f_L = 1$, $D_2 = -1$, $D_f = 1$, $M_\delta = -1$ for $T < 0$, $M_\delta = -10$ for $T > 0$, $M_\gamma = 1$, and $\mathcal{G} = -0.25$. The initial optical field ψ is calculated using Eq. (B1) of appendix B.

that the adiabatic approximation is applicable [see Eqs. (C5) and (C9) in appendix C]. For the more general case, NLSE (3) was numerically integrated. The color-coded plot in Fig. 4(d) presents the numerically calculated optical intensity $|\psi|^2$ as a function of time T and the retarded time t . For this calculation, it is assumed that the SPM coefficient M_δ abruptly changes at time $T = 0$. Values of other parameters are listed in the figure caption. The plot shown in Fig. 4(d) demonstrates that an abrupt change in the nonlinear response can give rise to narrowing, which mimics the experimental results shown in (b) and (c) of Fig. 4. A possible mechanism, which may provide such an abrupt change in the nonlinear response, is a 980 nm two-photon absorption occurring in the EDF [46, 47]. In addition, the experimentally-

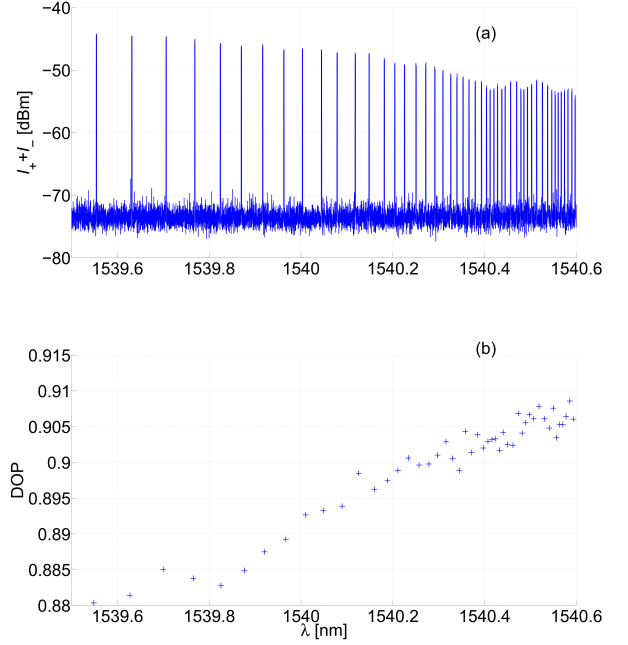


FIG. 5: DOP. The temperature is 3.5 K, and the diode current is $I_D = 0.3$ A. The DOP is plotted in (b) for all USOC peaks shown in (a).

observed narrowing occurring during the decay process can be attributed to pumping-induced widening effect [48].

DOP – The POSA instrument, which is attached to the fiber loop [see Fig. 1(a)], allows determining the polarization state of individual USOC peaks [25]. DOP that is extracted from the POSA data is displayed in Fig. 5(b), for each of the USOC peaks shown in Fig. 5(a). For this measurement, DOP values of about 0.9 are obtained [see Fig. 5(b)]. Much lower DOP values of about 0.12 are obtained when the PF is removed from the loop. As is demonstrated in the next section, the relatively high DOP enables some useful applications.

RF signal generation – Consider two USOC peaks having wavelengths λ and $\lambda + \delta\lambda$, respectively. The beating frequency f_b corresponding to this pair is $f_b = (c/\lambda^2) \delta\lambda + O(\delta\lambda^2)$, where, in the optical band in which USOC occurs, i.e., for $\lambda \simeq 1540$ nm, $c/\lambda^2 \simeq 0.126$ GHz nm $^{-1}$. The plots shown in Fig. 6 demonstrate an RFSA detection of USOC pairs' coherent beating. For these measurements the OF is installed between the 10:90 OC and the PD [see Fig. 1(a)]. Note that, in addition, an optical amplifier [not shown in the sketch in Fig. 1(a)] is added between the OF and the PD (to improve the signal-to-noise ratio). The two overlaid vertical dashed red lines in Fig. 6(a) denote the OF central wavelength λ_F for the plot shown in (b), for which $\lambda_F = 1539.7$ nm, and (c), for which $\lambda_F = 1539.9$ nm. The two nearest-neighbors USOC peaks have the beating fre-

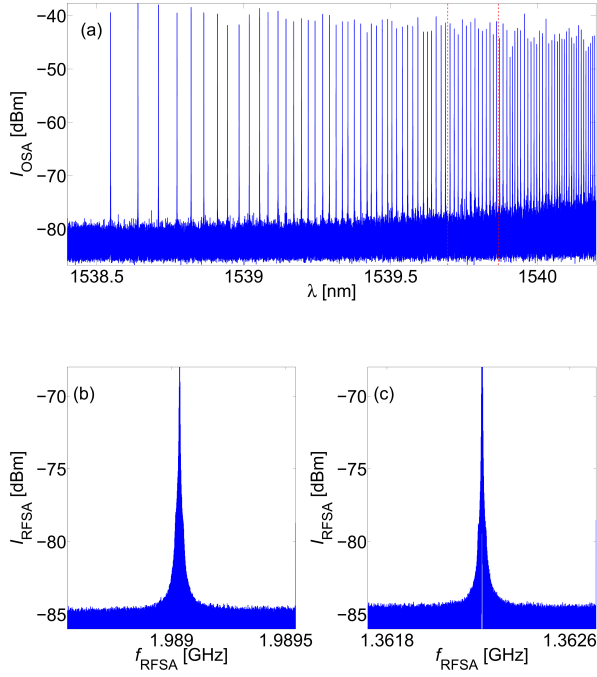


FIG. 6: RFSA. The temperature is 2.9 K, and the diode current is $I_D = 0.15$ A. The left and right overlaid red vertical dashed lines in (a) label the OF wavelength λ_F used for the RFSA measurements shown in (b) and (c), respectively. In (b) and (c), the averaging time is 25 minutes.

quency $f_b = 1.989037$ GHz and $f_b = 1.362216$ GHz, for (b) and (c), respectively. The plots in (b) and (c) display the RFSA spectral density I_{RFSA} averaged over 25 minutes. For both (b) and (c), variation in the peak frequency is about 10 kHz over this averaging period of 25 minutes. This frequency beating variation is partially attributed to temperature fluctuations in the fiber-loop section outside the cryostat.

Summary – Further study is needed to reveal the underlying mechanism responsible for the USOC formation. The device under the study allows a fully-tunable multi-mode lasing regime with enhanced DOP and high stability. These unique properties may open the way for novel USOC-based applications to fields including spectroscopy, communications, and quantum data storage.

Disclosures – The authors declare no conflicts of interest.

Appendix A: The nonlinear Schrödinger equation (NLSE)

The optical wave is represented by a state vector $|\psi(t', T)\rangle$, which depends on the retarded time t' and on full time T . The dynamics are governed by the NLSE,

$$i \frac{d|\psi\rangle}{dT} = H |\psi\rangle, \quad (\text{A1})$$

where $H = \mathcal{H} + i\Theta$, and both \mathcal{H} and Θ are Hermitian, i.e. $\mathcal{H}^\dagger = \mathcal{H}$ and $\Theta^\dagger = \Theta$. The state vector is represented by a wavefunction $\psi(t', T)$ given by $\psi(t', T) = \langle t' | \psi \rangle$, where the state $|t'\rangle$ represents an optical wave localized at the retarded time t' , i.e., $\langle t'' | t' \rangle = \delta(t' - t'')$. The operators \mathcal{H} and Θ are $\mathcal{H} = f_L (-D_2 p^2 + M_\delta \mathcal{N}(|\psi\rangle))$ and $\Theta = f_L (\mathcal{G} - D_f p^2 + M_\gamma \mathcal{N}(|\psi\rangle))$, where f_L is the loop frequency, D_2 is group delay dispersion (GDD), M_δ is the self-phase modulation (SPM), \mathcal{G} is the net gain (i.e., the gain minus loss), D_f is the filter dispersion, and M_γ is the nonlinear gain. The “momentum” operator p satisfies the relation $\langle t' | p | \psi \rangle = -i \partial \psi / \partial t'$, and the $|\psi\rangle$ -dependent operator $\mathcal{N}(|\psi\rangle)$ is $\mathcal{N}(|\psi\rangle) = \int dt'' |\langle t'' | \psi \rangle|^2 |t''\rangle \langle t''|$. Multiplying the generalized Schrödinger equation from the left by $\langle t' |$ yields Eq. (3). The following relation holds, $f_L^{-1} H = i\mathcal{G} - D p^2 + M \mathcal{N}(|\psi\rangle)$, where $D = D_2 + iD_f$ and $M = M_\delta + iM_\gamma$. Note that the Dirac’s notation is employed above just for convenience, while the optical wave is treated classically.

Appendix B: Dissipative soliton

The NLSE (3) has a dissipative-soliton solution [49–51]

$$\psi = \frac{\sqrt{\frac{W}{2t_p}}}{\cosh \frac{t}{t_p}} \exp \left[i \left(\beta \log \left(\frac{1}{\cosh \frac{t}{t_p}} \right) + \eta f_L T \right) \right], \quad (\text{B1})$$

where the chirp real coefficient β is given by

$$\beta = \frac{-3\chi \pm \sqrt{9\chi^2 + 8}}{2}, \quad (\text{B2})$$

with

$$\frac{1}{\chi} = \frac{\frac{D_2}{D_f} - \frac{M_\delta}{M_\gamma}}{\frac{D_2}{D_f} \frac{M_\delta}{M_\gamma} + 1}, \quad (\text{B3})$$

and the real variables t_p and η satisfy the following relations

$$\frac{2\beta D_f - (1 - \beta^2) D_2}{t_p^2} = \eta, \quad (\text{B4})$$

$$\frac{-2\beta D_2 - (1 - \beta^2) D_f}{t_p^2} = \mathcal{G}. \quad (\text{B5})$$

The energy corresponding to the dissipative solution is W , i.e., $\int_{-\infty}^{\infty} dt |\psi|^2 = W$ [see Eq. (B1)]. Note that the chirp coefficient vanishes, i.e. $\beta = 0$, for both extreme cases $M_\delta = D_2 = 0$ and $M_\gamma = D_f = 0$ [see Eqs. (B2) and (B3)]. For the former case $t_p = 4D_f / (WM_\gamma)$, and for the later one $t_p = 4D_2 / (WM_\delta)$.

The complex NLSE (3) has non-diverging stable steady-state solutions, provided that the damping is sufficiently strong. For the region where the complex NLSE (3) becomes unstable, a finite and stable steady-state solution can be obtained, provided that the gain-saturation

effect is taken into account. When the gain-relaxation time is long compared to f_L^{-1} , this effect is commonly accounted for by assuming that \mathcal{G} is a function of the total energy [39]. Alternatively, the stability can be restored by implementing the fixed-energy approximation. In this approximation, it is assumed that the total energy $\int_{-\infty}^{\infty} dt' |\psi(t', T)|^2$ is T -independent. This approximation can be implemented, by replacing NLSE (A1) by a modified one [52]

$$i \frac{d|\psi\rangle}{dT} = \left(\mathcal{H} + i\Theta - i \frac{\langle \psi | \Theta | \psi \rangle}{\langle \psi | \psi \rangle} \right) |\psi\rangle. \quad (\text{B6})$$

The term added to Eq. (B6) [compare with Eq. (A1)] ensures that norm conservation condition $0 = (d/dT) \langle \psi | \psi \rangle$ is satisfied.

Appendix C: The case $D_f = 0$ and $M_\gamma = 0$

For the case where both D and M are pure real, the NLSE (3) becomes

$$i \frac{d\psi}{dT} = f_L \left(i\mathcal{G} + D_2 \frac{\partial^2}{\partial t^2} + M_\delta |\psi|^2 \right) \psi. \quad (\text{C1})$$

We consider the case when \mathcal{G} , D_2 and M_δ are allowed to be T dependent. For this case, the total energy $W = \int_{-\infty}^{\infty} dt |\psi|^2$ evolves according to [see Eq. (A1)]

$$\frac{dW}{dT} = 2f_L \mathcal{G}(T) W. \quad (\text{C2})$$

Consider the case where D_2 and M_δ are both negative and slowly varying functions of T . In the framework of the adiabatic perturbation theory, the soliton solution is looked for as

$$\psi_A(t, T) = \frac{A(T) \exp\left(\frac{i}{2} \int_0^T dT' v^2(T')\right)}{\cosh\left(\frac{v(T)t}{\sqrt{-2f_L D_2(T)}}\right)}, \quad (\text{C3})$$

where $v(T)$ is real, and the soliton's amplitude is

$$A(T) = \frac{v(T)}{\sqrt{-f_L M_\delta(T)}}. \quad (\text{C4})$$

The energy W of the approximate ansatz (C3) is

$$W(T) = -\frac{2\sqrt{-\frac{2D_2(T)}{f_L}} v(T)}{M_\delta(T)}. \quad (\text{C5})$$

The approximate soliton solution (C3) is valid under the weak-gain condition

$$|\mathcal{G}(T)| \ll |M_\delta(T)| A^2(T). \quad (\text{C6})$$

In addition to this condition, the validity condition for the adiabatic approximation is

$$T_0 v^2(T) \gg 1, \quad (\text{C7})$$

where T_0 is a characteristic scale of the variation of the GDD and nonlinearity coefficients (in the case of constant coefficients, $T_0 = \infty$).

In the adiabatic approximation, the evolution of $v(T)$ is governed by

$$\frac{d \log v}{dT} = 2f_L \mathcal{G}. \quad (\text{C8})$$

The soliton's peak power $P(T) \equiv -v^2(T) / (f_L M_\delta(T))$ is obtained by the integration of Eq. (C8)

$$\frac{P(T)}{P(T=0)} = \frac{M_\delta(T=0)}{M_\delta(T)} \exp\left(4f_L \int_0^T dT' \mathcal{G}(T')\right). \quad (\text{C9})$$

Note that, in the adiabatic approximation, we have $W^2/P = 8D_2(T)/M_\delta(T)$ [see Eq. (C5)].

Appendix D: Mode expansion

The Fourier expansion of $\psi(t, T)$ as

$$\psi(t, T) = \sum_m a_m(z) e^{imx}, \quad (\text{D1})$$

where $z = f_L T$ and $x = \omega_L t$, yields [see Eq. (3)]

$$i\dot{a}_m = i\mathcal{G}a_m - D\omega_L^2 m^2 a_m + M \sum_{m' - m'' + m''' = m} a_{m'} a_{m''}^* a_{m'''}^*, \quad (\text{D2})$$

where $\omega_L = 2\pi f_L$ (the loop angular frequency), and the overdot denotes a derivative with respect to z .

To continue the analysis, we introduce the Wirtinger derivative ∂_m and its conjugate ∂_m^* , which are defined by $\partial_m = (1/2)(\partial/\partial\alpha_m - i\partial/\partial\beta_m)$ and $\partial_m^* = (1/2)(\partial/\partial\alpha_m + i\partial/\partial\beta_m)$, respectively, where the complex m -th mode amplitude a_m is expressed as $a_m = \alpha_m + i\beta_m$, and both α_m and β_m are real. The set of coupled equations of motion (D2) can be expressed in terms of the derivatives ∂_m^* as [53]

$$\dot{a}_m = -\partial_m^* \mathbb{H}, \quad (\text{D3})$$

where $\mathbb{H} = \mathbb{H}_1 + i\mathbb{H}_2$, and the real \mathbb{H}_1 and imaginary \mathbb{H}_2 parts are given by

$$\mathbb{H}_1 = -\mathcal{G}Q_1 + D_f \omega_L^2 Q_2 - \frac{M_\gamma}{2} Q_3, \quad (\text{D4})$$

$$\mathbb{H}_2 = -D_2 \omega_L^2 Q_2 + \frac{M_\delta}{2} Q_3, \quad (\text{D5})$$

where

$$Q_1 = \sum_{m'} a_{m'}^* a_{m'}, \quad (\text{D6})$$

$$Q_2 = \sum_{m'} m'^2 a_{m'}^* a_{m'}, \quad (\text{D7})$$

$$Q_3 = \sum_{m' - m'' + m''' - m'''' = 0} a_{m'} a_{m''}^* a_{m'''}^* a_{m''''}^*. \quad (\text{D8})$$

Appendix E: Steady state

Noise can be accounted for by replacing Eq. (D3) by

$$\dot{a}_m = -\partial_m^* \mathbb{H} + \xi_m, \quad (\text{E1})$$

where the added term ξ_m on the right-hand side of Eq. (E1) represents random noise with a vanishing averaged value. We consider the case with $D_2/D_f = M_\delta/M_\gamma$. For that case, and in the weak-noise limit, \mathbb{H}_1 is locally minimized in the steady state [see, e.g., Eq. (7.258) in [54]]. Henceforth, it is further assumed that both dispersion and SPM may be disregarded, i.e. $D = 0$ and $M_\delta = 0$. These assumptions yield $\mathbb{H} = \mathbb{H}_1 = -\mathcal{G}Q_1 - (1/2)M_\gamma Q_3$.

Note that the term Q_1 (D6) represents the total optical intensity. In the fixed-intensity approximation it is assumed that Q_1 is a constant (which is determined by the pump power). In this approximation, the term Q_3 in the function \mathbb{H}_1 can be replaced by $Q_3 - Q_1^2$ (note that constant terms in \mathbb{H} do not affect the time evolution). The following relation holds: $Q_3 = \sum_{\bar{n} \in S_c} a_{n'} a_{n''}^* a_{n'''} a_{n''''}^*$ [see Eq. (D8)] and $Q_1^2 = \sum_{\bar{n} \in S_d} a_{n'} a_{n''}^* a_{n'''} a_{n''''}^*$ [see Eq. (D6)], where $\bar{n} = (n', n'', n''', n''')$ denotes a quadruple of integers, the set $S_c \subset \mathbb{Z}^4$ is given by $S_c = \{(n', n'', n''', n''') \in \mathbb{Z}^4 | n' - n'' + n''' - n'''' = 0\}$, and the set $S_d \subset \mathbb{Z}^4$ is given by $S_d = \{(n', n'', n''', n''') \in \mathbb{Z}^4 | (n', n'') = (n''', n''')\}$ (\mathbb{Z} denotes the set of all integers), and thus (the symbol \setminus denotes set subtraction)

$$Q_3 - Q_1^2 = \sum_{\bar{n} \in S_c \setminus S_d} a_{n'} a_{n''}^* a_{n'''} a_{n''''}^*. \quad (\text{E2})$$

For the evaluation of the term $Q_3 - Q_1^2$ given by Eq. (E2), it is useful to notice that the frequency spacings between pairs of USOC peaks are all unique. Consider a quadruple of USOC peaks having mode indices m' , m'' , m''' , and m'''' . The empirical law given by Eq. (1) yields

$$i_{m'} - i_{m''} + i_{m'''} - i_{m''''} = \nu \log \frac{p_{m'} p_{m''''}}{p_{m''} p_{m'''}} , \quad (\text{E3})$$

where $i_m = (f_0 - f_m)/f_L$ is the normalized frequency detuning of the m -th mode. Note that $i_{m'} - i_{m''} + i_{m'''} - i_{m''''}$ is proportional to $m' - m'' + m''' - m''''$, and thus the fundamental theorem of arithmetics together with Eq. (E3) imply that

$$\bar{m} \equiv (m', m'', m''', m''') \notin S_c \setminus S_d, \quad (\text{E4})$$

provided that the pre-factor ν in Eq. (1) is sufficiently large. In other words, the term $Q_3 - Q_1^2$ [see Eq. (E2)] vanishes when USOC is formed. Hence, the contribution of the intermode coupling to \mathbb{H}_1 is minimized when USOC is formed, provided that $M_\gamma < 0$, i.e., RSA occurs in the USOC band (note that, generally, $Q_3 - Q_1^2$ is non-negative). However, the applicability of the above-discussed argument, which is based on the simplifying assumption that the dispersion may be disregarded (in the band where USOC occurs), is questionable, as it is not supported by dispersion measurements performed with the system under the study in an open-loop configuration [see Fig. (6) in [26]].

-
- [1] E Desurvire, JL Zyskind, and JR Simpson, "Spectral gain holeburning at 1.53 μm in erbium-doped fiber amplifiers", *IEEE Photon. Technol. Lett.*, vol. 2, no. 4, pp. 246–248, 1990.
 - [2] Masataka Nakazawa, Kazunori Suzuki, Hirokazu Kubota, and Yasuo Kimura, "Self-q-switching and mode locking in a 1.53- μm fiber ring laser with saturable absorption in erbium-doped fiber at 4.2 K", *Optics letters*, vol. 18, no. 8, pp. 613–615, 1993.
 - [3] Luc Thevenaz, Alexandre Fellay, Massimo Facchini, Walter Scandale, Marc Nikles, and Philippe A Robert, "Brillouin optical fiber sensor for cryogenic thermometry", in *Smart Structures and Materials 2002: Smart Sensor Technology and Measurement Systems*. International Society for Optics and Photonics, 2002, vol. 4694, pp. 22–27.
 - [4] Andrey Kobaykov, Michael Sauer, and Dipak Chowdhury, "Stimulated brillouin scattering in optical fibers", *Advances in optics and photonics*, vol. 2, no. 1, pp. 1–59, 2010.
 - [5] Julien Le Gouët, Jérémy Oudin, Philippe Perrault, Alaeddine Abbes, Alice Odier, and Alizée Dubois, "On the effect of low temperatures on the maximum output power of a coherent erbium-doped fiber amplifier", *Journal of Lightwave Technology*, vol. 37, no. 14, pp. 3611–3619, 2019.
 - [6] Marine Aubry, Luciano Mescia, Adriana Morana, Thierry Robin, Arnaud Laurent, Julien Mekki, Emmanuel Marin, Youcef Ouerdane, Sylvain Girard, and Aziz Boukenter, "Temperature influence on the radiation responses of erbium-doped fiber amplifiers", *physica status solidi (a)*, vol. 218, no. 15, pp. 2100002, 2021.
 - [7] Qi Xi, Shihai Wei, Chenzhi Yuan, Xueying Zhang, You Wang, Haizhi Song, Guangwei Deng, Bo Jing, Daniel Oblak, and Qiang Zhou, "Experimental observation of coherent interaction between laser and erbium ions ensemble doped in fiber at sub 10 mK", *Science China Information Sciences*, vol. 63, pp. 1–7, 2020.
 - [8] Shi-Hai Wei, Bo Jing, Xue-Ying Zhang, Jin-Yu Liao, Hao Li, Li-Xing You, Zhen Wang, You Wang, Guang-Wei Deng, Hai-Zhi Song, et al., "Storage of 1650 modes of single photons at telecom wavelength", *arXiv:2209.00802*, 2022.
 - [9] Antonio Ortu, Jelena V Rakonjac, Adrian Holzäpfel, Alessandro Seri, Samuele Grandi, Margherita Mazzera, Hugues de Riedmatten, and Mikael Afzelius, "Multi-mode capacity of atomic-frequency comb quantum memories", *Quantum Science and Technology*, vol. 7, no. 3, pp. 035024, 2022.
 - [10] Duan-Cheng Liu, Pei-Yun Li, Tian-Xiang Zhu, Liang

- Zheng, Jian-Yin Huang, Zong-Quan Zhou, Chuan-Feng Li, and Guang-Can Guo, “On-demand storage of photonic qubits at telecom wavelengths”, *arXiv:2201.03692*, 2022.
- [11] Mahdi Bornadel, Sara Shafiei Alavijeh, Farhad Rasekh, Nasser Gohari Kamel, Faezeh Kimiaee Asadi, Erhan Saglamyurek, Daniel Oblak, and Christoph Simon, “Hole burning experiments and modeling in erbium-doped silica glass fibers down to millikelvin temperatures: evidence for ultra-long population storage”, *arXiv:2412.16013*, 2024.
 - [12] Wolfgang Tittel, Mikael Afzelius, Adam Kinoshita, Lars Rippe, and Andreas Walther, “Quantum networks using rare-earth ions”, *arXiv:2501.06110*, 2025.
 - [13] Bo Jing, Shihai Wei, Longyao Zhang, Dianli Zhou, Yuxing He, Xihua Zou, Wei Pan, Hai-Zhi Song, and Lianshan Yan, “Approaching scalable quantum memory with integrated atomic devices”, *Applied Physics Reviews*, vol. 11, no. 3, pp. 031304, 2024.
 - [14] Shobhit Gupta, Xuntao Wu, Haitao Zhang, Jun Yang, and Tian Zhong, “Robust millisecond coherence times of erbium electron spins”, *Physical Review Applied*, vol. 19, no. 4, pp. 044029, 2023.
 - [15] Erhan Saglamyurek, Thomas Lutz, Lucile Veissier, Morgan P Hedges, Charles W Thiel, Rufus L Cone, and Wolfgang Tittel, “Efficient and long-lived zeeman-sublevel atomic population storage in an erbium-doped glass fiber”, *Physical Review B*, vol. 92, no. 24, pp. 241111, 2015.
 - [16] Sara Shafiei, Erhan Saglamyurek, and Daniel Oblak, “Hour-long decay-time of erbium spins in an optical fiber at milli-kelvin temperatures”, in *Quantum Information and Measurement*. Optical Society of America, 2021, pp. F2A-4.
 - [17] Hermann Haken, *Laser light dynamics*, vol. 1, North-Holland Amsterdam, 1985.
 - [18] Andriy O Semenov, Serhii Tsyrlunyk, Olena O Semenova, Serhii Baraban, and Anton Khloba, “Dynamic random access memory based on fiber optic lines for optical computers. computer modeling.”, in *COLINS (2)*, 2024, pp. 23–34.
 - [19] S Yamashita and K Hotate, “Multiwavelength erbium-doped fibre laser using intracavity etalon and cooled by liquid nitrogen”, *Electronics Letters*, vol. 32, no. 14, pp. 1298–1299, 1996.
 - [20] Haochong Liu, Wei He, Yantao Liu, Yunhui Dong, and Lianqing Zhu, “Erbium-doped fiber laser based on femtosecond laser inscribed fbg through fiber coating for strain sensing in liquid nitrogen environment”, *Optical Fiber Technology*, vol. 72, pp. 102988, 2022.
 - [21] J Lopez, H Kerbertt, M Plata, E Hernandez, and S Stepanov, “Two-wave mixing in erbium-doped-fibers with spectral-hole burning at 77k”, *Journal of Optics*, vol. 22, no. 8, pp. 085401, 2020.
 - [22] Eyal Buks, “Tunable multimode lasing in a fiber ring”, *Physical Review Applied*, vol. 19, no. 5, pp. L051001, 2023.
 - [23] Martin Hofer, MH Ober, F Haberl, and ME Fermann, “Characterization of ultrashort pulse formation in passively mode-locked fiber lasers”, *IEEE journal of quantum electronics*, vol. 28, no. 3, pp. 720–728, 1992.
 - [24] ME Fermann, MJ Andrejco, Y Silberberg, and ML Stock, “Passive mode locking by using nonlinear polarization evolution in a polarization-maintaining erbium-doped fiber”, *Optics letters*, vol. 18, no. 11, pp. 894–896, 1993.
 - [25] Eyal Buks, “Polarimeter optical spectrum analyzer”, *Photonics*, vol. 11, no. 6, pp. 486, 2024.
 - [26] Eyal Buks, “Intermode coupling in a fiber loop laser at low temperatures”, *Journal of Lightwave Technology*, vol. 42, pp. 2951, 2024.
 - [27] Pierluigi Franco, Michele Midrio, A Tozzato, Marco Romagnoli, and F Fontana, “Characterization and optimization criteria for filterless erbium-doped fiber lasers”, *JOSA B*, vol. 11, no. 6, pp. 1090–1097, 1994.
 - [28] Sonia Melle, Oscar G Calderón, Miguel A Antón, Fernando Carreno, and Ana Egatz-Gómez, “Spectral hole burning in erbium-doped fibers for slow light”, *JOSA B*, vol. 29, no. 8, pp. 2189–2198, 2012.
 - [29] Markus P Hehlen, Nigel J Cockroft, TR Gosnell, and Allan J Bruce, “Spectroscopic properties of Er^{3+} - and Yb^{3+} -doped soda-lime silicate and aluminosilicate glasses”, *Physical Review B*, vol. 56, no. 15, pp. 9302, 1997.
 - [30] Sara Shafiei Alavijeh, “Hole burning spectroscopy of erbium-doped optical fibre for applications in quantum networks”, 2022.
 - [31] SMJ Kelly, “Characteristic sideband instability of periodically amplified average soliton”, *Electronics Letters*, vol. 28, no. 8, pp. 806–807, 1992.
 - [32] James P Gordon, “Dispersive perturbations of solitons of the nonlinear schrödinger equation”, *JOSA B*, vol. 9, no. 1, pp. 91–97, 1992.
 - [33] Govind P Agrawal, “Nonlinear fiber optics”, in *Nonlinear Science at the Dawn of the 21st Century*, pp. 195–211. Springer, 2000.
 - [34] Yung-Hsiang Lin and Gong-Ru Lin, “Kelly sideband variation and self four-wave-mixing in femtosecond fiber soliton laser mode-locked by multiple exfoliated graphite nano-particles”, *Laser Physics Letters*, vol. 10, no. 4, pp. 045109, 2013.
 - [35] Yaroslav V Kartashov, Boris A Malomed, and Lluís Torner, “Solitons in nonlinear lattices”, *Reviews of Modern Physics*, vol. 83, no. 1, pp. 247–305, 2011.
 - [36] Boris A Malomed, “New findings for the old problem: Exact solutions for domain walls in coupled real ginzburg-landau equations”, *Physics Letters A*, vol. 422, pp. 127802, 2022.
 - [37] Herman A Haus, “Mode-locking of lasers”, *IEEE Journal of Selected Topics in Quantum Electronics*, vol. 6, no. 6, pp. 1173–1185, 2000.
 - [38] M Montagna, S Selleri, and M Zoboli, “Nonlinear refractive index in erbium-doped optical amplifiers”, *Optical and quantum electronics*, vol. 27, pp. 871–880, 1995.
 - [39] Deeksha Jachpure and R Vijaya, “Saturable absorption and its consequent effects in bistable erbium-doped fiber ring laser”, *Journal of Optics*, vol. 24, no. 2, pp. 024007, 2022.
 - [40] Yoshinobu Maeda, “Mechanism of the negative nonlinear absorption effect in a five-level system of the Er^{3+} ion”, *Journal of applied physics*, vol. 83, no. 3, pp. 1187–1194, 1998.
 - [41] Todd Kapitula, J Nathan Kutz, and Björn Sandstede, “Stability of pulses in the master mode-locking equation”, *JOSA B*, vol. 19, no. 4, pp. 740–746, 2002.
 - [42] Michael L Dennis and Irl N Duling, “Experimental study of sideband generation in femtosecond fiber lasers”, *IEEE Journal of Quantum electronics*, vol. 30, no. 6, pp. 1469–1477, 1994.
 - [43] Shen Huang, Guodong Shao, Yufeng Song, Luming Zhao,

- Deyuan Shen, and Dingyuan Tang, “Dark solitons embedded in a stable periodic pulse train emitted by a fiber ring laser”, *Journal of Physics: Photonics*, vol. 2, no. 3, pp. 034009, 2020.
- [44] Gang Wang, Yuxuan Ma, Ce Shang, Haojing Huang, Zherui Lu, Shuaixin Wang, Jingxuan Sun, Chenghong Zhang, and Bo Fu, “Influence of reverse saturable absorption effect on conventional and dissipative solitons fiber lasers”, *Optics & Laser Technology*, vol. 137, pp. 106805, 2021.
- [45] Rongfei Wei, Hang Zhang, Xiangling Tian, Tian Qiao, Zhongliang Hu, Zhi Chen, Xin He, Yongze Yu, and Jianrong Qiu, “Mos 2 nanoflowers as high performance saturable absorbers for an all-fiber passively q-switched erbium-doped fiber laser”, *Nanoscale*, vol. 8, no. 14, pp. 7704–7710, 2016.
- [46] Peter A Krug, Mark G Sceats, GR Atkins, SC Guy, and Simon B Poole, “Intermediate excited-state absorption in erbium-doped fiber strongly pumped at 980 nm”, *Optics letters*, vol. 16, no. 24, pp. 1976–1978, 1991.
- [47] Gui Xiao, Ghazal Fallah Tafti, Amirhassan Zareanborji, Anahita Ghaznavi, and Qiancheng Zhao, “Measurement of active optical fibers”, in *Handbook of Optical Fibers*, pp. 1–38. Springer, 2019.
- [48] Masataka Nakazawa, Hirokazu Kubota, Akio Sahara, and Kohichi Tamura, “Time-domain abcd matrix formalism for laser mode-locking and optical pulse transmission”, *IEEE Journal of Quantum Electronics*, vol. 34, no. 7, pp. 1075–1081, 1998.
- [49] N.R. Pereira and Lennart Stenflo, “Nonlinear schrodinger equation including growth and damping”, *The Physics of Fluids*, vol. 20, pp. 1733, 1977.
- [50] Oscar E Martínez, Richard L Fork, and James P Gordon, “Theory of passively mode-locked lasers for the case of a nonlinear complex-propagation coefficient”, *Journal of the Optical Society of America B*, vol. 2, no. 5, pp. 753–760, 1985.
- [51] Hermann A Haus, James G Fujimoto, and Erich P Ippen, “Structures for additive pulse mode locking”, *Journal of the Optical Society of America B*, vol. 8, no. 10, pp. 2068–2076, 1991.
- [52] Eyal Buks, “Spontaneous disentanglement and thermalization”, *Advanced Quantum Technologies*, p. 2400036, 2024.
- [53] Zied Ammari and Vedran Sohinger, “Gibbs measures as unique kms equilibrium states of nonlinear hamiltonian pdes”, *Revista Matemática Iberoamericana*, vol. 39, no. 1, pp. 29–90, 2022.
- [54] Eyal Buks, *Statistical physics - Lecture Notes*, <http://buchs.net.technion.ac.il/teaching/>, 2025.